Int. J. Nano Dimens., 13 (2): 155-167, Spring 2022

ORIGINAL ARTICLE

Hirshfeld surface analysis of solid-state synthesized $NiFe_2O_4$ nanocomposite and application of it for photocatalytic degradation of Water pollutant dye

Alireza Hakimyfard[1,*], *Shahin Khademinia*[2]

[1] *Department of Physics, Faculty of Science, Jundi-Shapur University of Technology, Dezful, Iran*
[2] *Department of Inorganic Chemistry, Faculty of Chemistry, Semnan University, Semnan, Iran*

Received 24 October 2021; revised 20 November 2021; accepted 27 November 2021; available online 30 November 2021

Abstract

The present work reports the Hirshfeld surface analysis and photocatalytic performance of $NiFe_2O_4$ nanomaterial. Hirshfeld surface analysis was performed to understand the interaction properties of the $NiFe_2O_4$ compound. The active sites including π-π interactions are studied by the analysis. The Hirshfeld data showed that the two wings in the O…O, and O…Ni diagrams are created by short contacts of O…O and O…Ni which causes O—O…π and O—Ni…. π interactions. The interactions cover the surfaces with values of 8.8% and 9.4%, respectively. Nanostructured $NiFe_2O_4$ powder was used as a photocatalyst to degrade Malachite Green (MG) waste water pollutant dye under visible light irradiation. The optimized conditions for the degradation of a 100 mL of 80 ppm MG aqueous solution are 0.03 mL H_2O_2, 0.038 g catalyst and 45 min reaction time. The degradation yield at the optimized conditions under visible light irradiation was 95 %. The light source was a white color fluorescent lamp with the 40 W power and light intensity of 1.34 W/m^2 measured by a digital lux meter.

Keywords: *Dye Degradation; Hirshfeld Surface Analysis; Malachite Green; Nanophotocatalyst; Nickel Ferrite.*

How to cite this article

Hakimyfard A., Khademinia Sh. Hirshfeld surface analysis of solid-state synthesized $NiFe_2O_4$ nanocomposite and application of it for photocatalytic degradation of Water pollutant dye. Int. J. Nano Dimens., 2022; 13(2): 155-167.

INTRODUCTION

Inverse spinel structured soft magnetic materials like nickel ferrite ($NiFe_2O_4$) are mixed metal oxides that have general formula MFe_2O_4 (M = divalent metal ion, e.g. Ni, Co, Cu, etc.) [1, 2]. $NiFe_2O_4$ exhibits a noncollinear spin structure in ultrathin form. $NiFe_2O_4$ is of interest for researchers because of its high magneto crystalline anisotropy, high saturation magnetization and unique magnetic structure [3-6]. $NiFe_2O_4$ shows different types of magnetic behaviour including paramagnetic, superparamagnetic or ferrimagnetic properties depending on the particle size and shape. The compound shows several applications in medicine such as magnetic resonance imaging, drug delivery, cancer therapies, telecommunications, high frequency transformers, and catalysts. $NiFe_2O_4$ is an n-type semiconductor and the Ni^{2+} ions are located at octahedral sites but the Fe^{3+} ions are located at both tetrahedral and octahedral sites [6-10]. MG is classified in the dyestuff industry as a triarylamine dye and used in pigment industry. MG has been used extensively in the leather, paper, silk, cotton, and jute dyeing processes. It is also used as an antifungal and anti-protozoan agent in fisheries and aquaculture industry [11, 12]. MG is a non-biodegradable dye pollutant and has now become a highly controversial compound due to the risks it poses to the consumers of treated fish, including its effects on the immune and reproduction systems. Furthermore, MG and its metabolites are known to cause mutagenic, carcinogenic, and teratogenic effects to living organisms [13]. It should not be used for beverages, food, medicines because it causes skin irritation, blurred vision or cause

* Corresponding Author Email: *ahakimyfard@jsu.ac.ir, ahakimyfard@yahoo.com*

interference. Its inhalation may cause irritation to the respiratory tract, and in large quantities can cause tissue damage and inflammation of kidneys [14]. Pure and functionalized metal oxides nanopowders have found several catalytic and photocatalytic applications [15,16]. Recently, several metal oxides have been used for the degradation of pollutant dyes under different conditions including: MoS_2/TiO_2 nanocomposite [17], $PbCrO_4$ [18], TiO_2/ZrO_2 [19], Ni_x:TiO_2 [20], TiO_2 [21], V doped ZnO [22], TiO_2 [23], $Ni_{1-x}Co_xFe_2O_4$ [24], $Pt/TiO_2/SiO_2$ [25], $Sr_2As_2O_7$ [26], SiO_2/CuS [27], $Mg_{1-x}Ni_xAl_2O_4$ [28], α-Fe_2O_3 [29], etc. Experimental design method is used to find optimum values of parameters affect on MG photodegradation conditions. In the method, a Design Of Expert (DOE) using Central Composite Design (CCD) is applied. In photocatalytic processes, Design of Expert software is used to help researchers to see how much a photocatalyst and H_2O_2 are used and how many minutes are needed to finalize the degradation process. The software offers a wide range of designs, including factorials, fractional factorials and composite designs. Design of Expert offers computer generated D-optimal designs for cases where standard designs are not applicable, or where we wish to augment an existing design [30, 31]. A Box-Wilson Central Composite Design, commonly called a central composite design (CCD), contains an imbedded factorial or fractional factorial design with center points that is augmented with a group of points that allow estimation of curvature. If the distance from the center of the design space to a factorial point is ±1 unit for each factor, the distance from the center of the design space to a point is $|\alpha| > 1$. The precise value of α depends on certain properties desired for the design and on the number of factors involved [30, 31]. The main purpose of the present work is introducing an efficient photocatalyst for degradation of waste water pollutant dye. Besides, theoretical calculation that studies the surface active sites on the photocatalyst crystal system is also focused. So, the intermolecular interactions in the crystal structure of $NiFe_2O_4$ are studied by Hirshfeld surface analysis. Also, the photocatalytic performance of the synthesized $NiFe_2O_4$ nanomaterial is investigated for the degradation of MG under visible light irradiation. Experimental design method is used to optimize factors affecting the degradation reaction. The factors are the amount of the nanocatalyst, H_2O_2 and the reaction time.

EXPERIMENTAL

General remarks

All chemicals were of analytical grade, obtained from commercial sources, and used without further purification. Hirshfeld surface (HS) analysis was done by Crystal Explorer Hirshfeld package. The Software used for the design of experiment (DOE) was Design Expert 7. Measurement of the photocatalytic activity of the synthesized samples was investigated in the presence of H_2O_2 (30%, w/w) under visible light source. A Shimadsu, UV-Vis 1650 PC spectrophotometer was used to measure the absorbance spectra of MG in the range of 200–700 nm by a quartz cell with an optical path of 1 cm. A BEL PHS-3BW pH-meter with a combined Glass-Ag/AgCl electrode was used for adjustment of test solution pH. A digital Lux meter model GM 1010 was used to measure the light intensity of the light used in the photocatalytic process.

Synthesis of $NiFe_2O_4$ nanomaterial

$NiFe_2O_4$ nanomaterial was fabricated by solid state method [32]. In a typical experiment, $NiFe_2O_4$ was prepared by the following procedure: 0.16 g, (1 mmole) of $FeCl_3$ (MW= 162.2 $gmole^{-1}$) and 0.15 g (0.5 mmole) of $Ni(NO_3)_2.6H_2O$ were used, ground and the obtained powder was treated thermally at 1000 ˚C for 24 h.

RESULTS AND DISCUSSIONS

Hirshfeld surface (HS) analysis

3D Hirshfeld surface's analysis (HS) of $NiFe_2O_4$ was made by Crystal Explorer 17.5 [33] which admits a structure input file with a crystal information file (CIF) format. d_{norm} is determined from the spacing between the nearest great atoms that is prominent at the surface of the Hirshfeld. The standard Cif file of $NiFe_2O_4$ was downloaded from crystallography.net website. The normalized contact distance's d_{norm} based on both d_e (distance from the point to the nearest nucleus external to the surface) and d_i (distance to the nearest nucleus internal to the surface) and the van der Waals (vdW) radii of the atom, defined using equation (1), that had been considered the area of special importance to intermolecular interactions [34]:

$$d_{norm} = \frac{d_i - r_i^{vdw}}{r_i^{vdw}} + \frac{d_e - r_e^{vdw}}{r_e^{vdw}}$$

Areas of varying intermolecular interactions that are of particular importance are identified in different red, blue, and white colors. Shorter contacts from the van der Waals radius are indicated by the negative (red) or longer contact with the positive (blue) and equal to or near the van der Waals radius by zero (white color) values of d_{norm}. The fingerprint plot using a distance of d_i and d_e has made a separate surface for each point, which displayed the information obtained from HS analysis briefly and quantitatively in two-dimensional grid plots [35, 36]. As well as the plot is available in a variety of blue, green, and red that represent low, medium, and high frequency are used for precise analysis, decomposed' FPs, and allow for the identification of different interaction. These decomposed fingerprint plots contain the two-sided X…L/L…X interactions in which X is positioned internal (for X…L/$d_e < d_i$) or external (for L…X/ $d_e > d_i$). The complementary areas, where one molecule is a donor ($d_e > d_i$) and the other as an acceptor ($d_e < d_i$), can be also identified in the fingerprint plots (FPs) [37].

Hirshfeld surface analysis $NiFe_2O_4$

The Hirshfeld surface analysis creates it easy to visualize the molecular part by enabling surface transparency using d_{norm}, d_i, $d_{e,}$ shape index, and curvedness. Hirshfeld surfaces corresponding generated from an atomic spherically averaged electron density. In Fig. 1 a-f, the intense red and light red spots on HS suggesting the strong interactions of the other intermolecular exchanges. According to Fig. 1 a-c, the donor area is flat surfaces and green. The intense red spot was observed on the Ni and O atoms confirming the presence of interaction via these atoms. The color code on Hirshfeld surfaces represents the geometrical d_{norm} function of $NiFe_2O_4$. The red spots in the d_{norm} surface illustrated predominant interatomic or shorter contacts (< vdW radii). It can be clearly seen from the figure that the interaction intensity map, the heavier the color of the red area, the stronger interactions, and the other shallower areas are mainly the distribution of short-range effects. Hirshfeld surfaces mapped over the curvedness is displayed in Fig. 1 d. The appearance of flat surfaces determined by a blue outline on $NiFe_2O_4$ cell in Hirshfeld surface mapped over curvedness obviously specifies the attendance of π···π interaction. In Fig. 1 e and f, the images displayed Hirshfeld surfaces mapped over the shape index function. In the Hirshfeld surface analysis mapped with a shape index function attendance of red and blue triangles (bow-tie pattern) highlighted clearly indicate the π···π interactions. The acceptor area was displayed with flat surfaces and red spots.

The fingerprint plots (d_i vs d_e plot) are shown in Fig. 2a-e. Fig. 2a represents the overall interactions of the component metal ions in the unit cell. According to the d_i vs d_e plot, the maximum

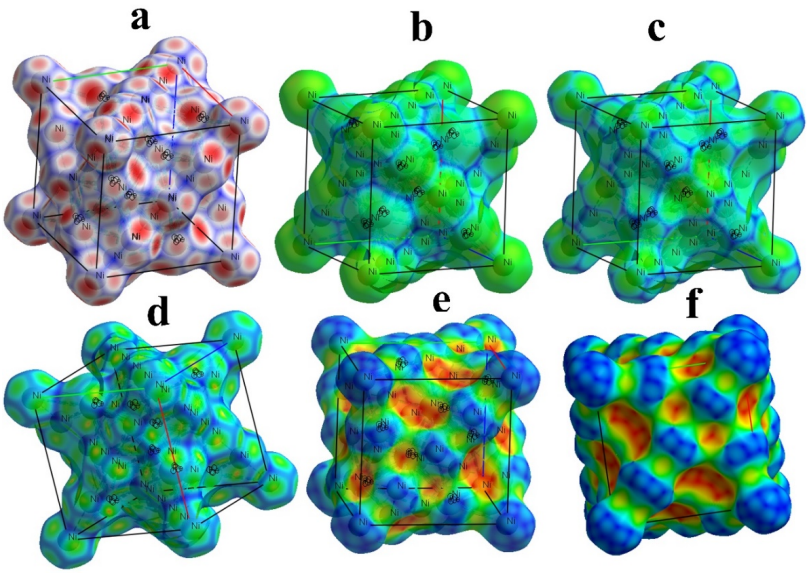

Fig. 1. Hirshfeld surfaces corresponding generated from an atomic spherically averaged electron density a) dnorm, b) de, c) di, d) curveness and e, f) shape index functions.

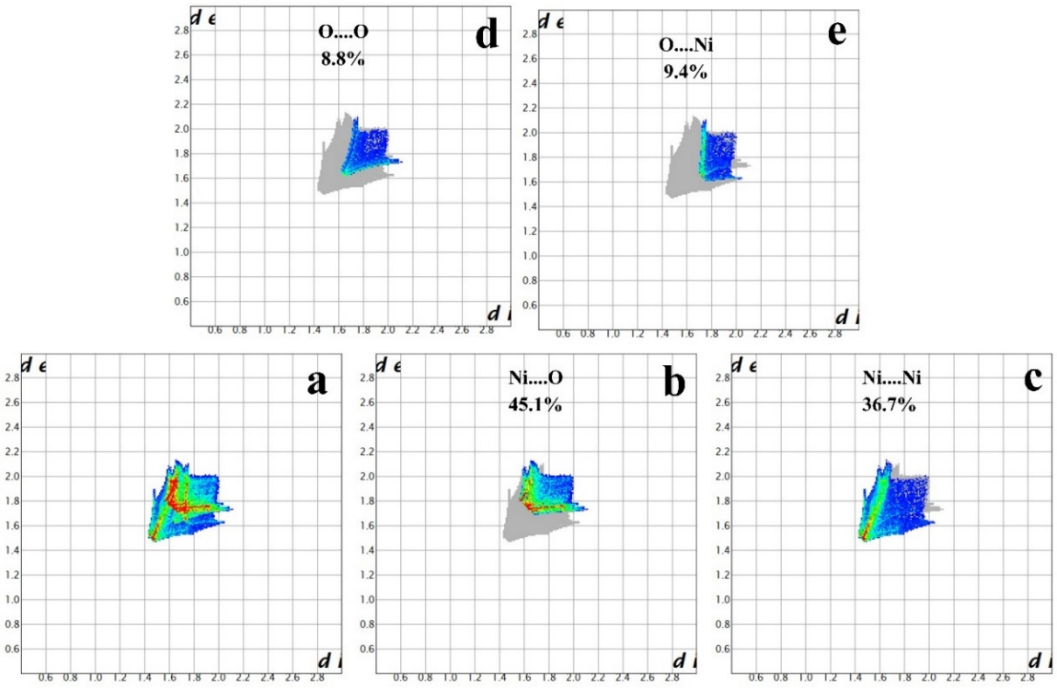

Fig. 2. a) whole interactions, b) Ni…O, c) Ni…Ni, d) O…O and e) O…Ni interactions 2D fingerprint plots generated from an atomic spherically averaged electron density for $NiFe_2O_4$.

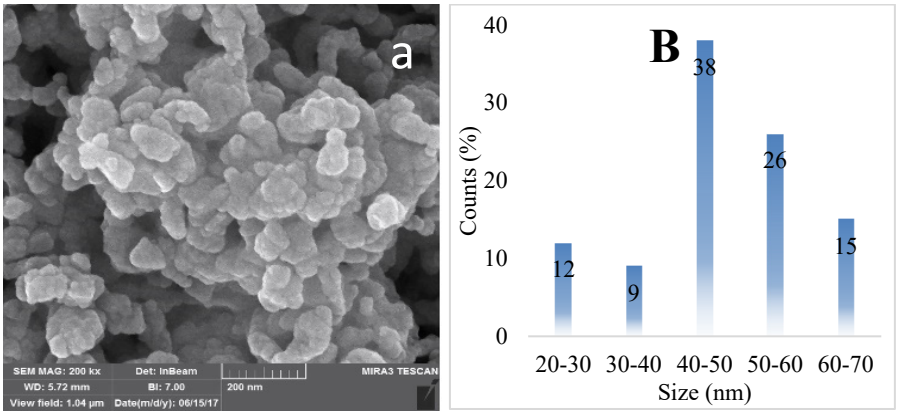

Fig. 3. a) FESEM image and b) particle size distribution profile of $NiFe_2O_4$ nanocomposite.

amounts of interactions are determined for Ni…O interactions (Fig. 2b), which cover a wide variety of Hirshfeld surface occupying 45.1% manifested by the points spread out in the center of fingerprint plots. Based on the fingerprint plots (d_i vs d_e plot) in Fig. 2 c, Ni—Ni contact with the percentage of the surface of 36.7% ($d_i + d_e$ » 3.0) is formed and compared with other contacts, which shows that it plays an important role in the crystalline formation. The two wings in the O…O and O…Ni diagrams (Fig. 2d and 2e, respectively)) are created from short contacts of O…O and O…Ni which causes interaction O—O…π and O—Ni…. π. The interactions cover the surfaces with values of 8.8% and 9.4%, respectively.

Morphology analysis

Fig. 3a and b presents FESEM image and particle size distribution profile of the as-prepared $NiFe_2O_4$ nanocomposite. As previously reported, $NiFe_2O_4$ has particle morphology with the average size of 40–50 nm. The particle size distribution profile indicates that the maximum distribution is at the range of 40-50 nm. However, it is found that

the composite is composed of particles with the diameters of 20-70 nm.

Photocatalytic activity

The photocatalytic activity of $NiFe_2O_4$ nanocomposite was investigated for the degradation of MG in the presence of H_2O_2 (30%, w/w) under visible light irradiation. To prepare 80 ppm MG dye solution, 80 mg of MG powder was dissolved in 1000 mL of deionized water. The pH value of the obtained solution was 4. In a typical photocatalytic experiment, certain amount (g) of the as-synthesized $NiFe_2O_4$ photocatalyst (0.03 g, for example) was added into 100 mL of the prepared MG aqueous solution at the room temperature (system temperature) and sonicated for 10 min in a dark room to establish an adsorption/desorption equilibrium between MG molecules and the surface of the photocatalyst. Afterwards, certain volume (mL) of H_2O_2 (0.03 mL, for example) were added into the mixture solution, followed by further magnetic stirring under visible light irradiation. When the designed time (min) was elapsed, the solution was drawn out and the photocatalyst was separated by centrifugation with the velocity of 100 rpm for 5 min in order to measure the absorption spectra of MG and calculate the MG concentration using UV-Vis spectrophotometry. The mixture was kept at a constant stirring of 300 rpm at the temperature of the experiment. The photodegradation yield (%) of MG was calculated by the following formula:

$$\left(\frac{A_0\text{-}A_t}{A_0}\right)\times 100 \qquad (7)$$

where, A_0 and A_t represent the initial absorbance of MG at 612 nm and the absorbance at time t, respectively.

Experimental design for achieving optimal conditions in MG degradation process

Researchers utilize two different approaches to obtain the optimal conditions in chemical reactions, namely one-at-a-time and experimental design methods. Recently, the experimental design method is receiving more attention. Full factorial design is one of the basic designs. In this design, all possible combinations of the factors and their settings are simultaneously considered. Assume that there is k investigating variables and each variable could be set to m distinctive levels. The number of possible combinations of the factors and their settings will then be m^k. In chemical systems, three levels of the factor setting are common because such designs allow the determination of all main effects and all interaction effects with small number of experiment.

Full factorial design is one of the most powerful design tools in which three levels of each factor are used to design a set of proposed runs. In this design, the experimental points are embedded at the center (central points) and on the midpoints of the edges. In full factorial method, the relation between the factors and response is theoretically modeled which causes the reproducibility of the results. So, it is possible for experiments to elucidate the results. Response surface methodology (RSM) is a mathematical and statistical method analyzing experimental design by applying an empirical model. The Response surface methodology (RSM) using input data, offers the graphical relationship between responses and variables, and performs multiple regression analysis [30, 31].

The adequacy of the applied model is checked using analysis of variance (ANOVA) which needs some replicate experiments.

In the present MG pollutant dye degradation process, the goal was to determine how much nanocatalyst should be used, and at which time and H_2O_2 volume the degradation should be monitored. The response was the yield of degradation (Y%). Different possible combinations of these factors were designed which are reported in Table 2. All the experiments were done at two days with random order. The central composite design (CCD) was chosen to model and optimize the proposed procedure. A three-level CCD with three factors (H_2O_2 (A), catalyst (B) and time (C)) was used to investigate the effects of factors. The condition of 20 experiments designed by CCD accompanied to dye degradation percentage (response (R%)) are also given in Table 1. The experimental range and levels of independent variables are shown in Table 2. As shown in table 2, the independent variables (H_2O_2 volume (A_1), catalyst amount (A_2) and stirring time (A_3)) are given in the coded form (-α, -1, 0, +1, +α).

The statistical test of ANOVA analyzes the variances and examines the significance of the factors and their interactions on themselves and other factors. Then, with the help of RSM, the validated model is plotted in three dimensions and interpreted to find the best conditions for

Table 1. Experimental and predicted results of applied model for photo-catalytic malachite green degradation over $NiFe_2O_4$.

H_2O_2	Catalyst	Time	Yield
0.01	0.04	45	60
0.01	0.01	15	15
0.01	0.01	45	36
0.03	0.04	45	90
0.03	0.04	15	75
0.02	0.025	30	65
0.02	0.025	30	65
0.01	0.04	15	40
0.03	0.01	15	25
0.02	0.025	30	65
0.02	0.025	30	65
0.03	0.01	45	56
0	0.025	30	20
0.02	0.025	30	66
0.02	0	30	12
0.02	0.025	55	80
0.02	0.025	30	68
0.02	0.050	30	83
0.02	0.025	5	12
0.04	0.025	30	70

Table 2. Ranges of operational parameters for experimental design in CCD.

Factor Name	Units	Low Actual	High Actual	Low Coded	High Coded
A	H_2O_2 (mL)	0.01	0.03	-1	1
B	Catalyst (mg)	0.01	0.04	-1	1
C	Time (min)	15	45	-1	1

Table 3. ANOVA test results for degradation of malachite green by photo-catalytic process.

Source	Sum of Squares	df	Mean Square	F-value	p-value	
Block	12.03	1	12.03			
Model	11874.37	9	1319.37	129.35	< 0.0001	significant
A-H_2O_2	2730.03	1	2730.03	267.65	< 0.0001	
B-Catalyst	5196.87	1	5196.87	509.49	< 0.0001	
C-Time	2647.12	1	2647.12	259.52	< 0.0001	
AB	120.13	1	120.13	11.78	0.0075	
AC	0.1250	1	0.1250	0.0123	0.9143	
BC	55.13	1	55.13	5.40	0.0451	
A^2	645.16	1	645.16	63.25	< 0.0001	
B^2	486.02	1	486.02	47.65	< 0.0001	
C^2	195.89	1	195.89	19.20	0.0018	
Residual	91.80	9	10.20			
Lack of Fit	65.05	5	13.01	1.95	0.2694	not significant
Pure Error	26.75	4	6.69			
Cor Total	11978.20	19				

the process. ANOVA of regression parameters for the quadratic model was computed in Table 3. The Fisher's F test in the ANOVA analysis was performed to compare either model variance or factors with residual (error) variance, where the larger F-values and the smaller P-values indicate the more significant terms of the model [30, 31]. This ratio is called an F-distribution (F-value), varying from 1 to larger values. Values far from 1, exceeding from the tabulated F-value, provide evidence against the null hypothesis, indicating the significance of the regression parts of the fitted models. Equivalently, the null hypothesis is rejected when p-value is less than a significant level. In order to obtain the significant and reliable model at 95% confidence level, the p-values for the fitted model and its corresponding terms should be smaller than 0.05. The p-value of

Table 4. Comparison study of the photocatalytic ability of the $NiFe_2O_4$ with some other catalysts [26].

	Catalyst	Condition	Yield (%)
1	**$NiFe_2O_4$ (Present Work)**	H_2O_2, 30 mg catalyst, 35 min, visible ligth, 70 mL of 45 ppm MG	95
1	**$Sr_2As_2O_7$**	H_2O_2, 20 mg catalyst, 33 min, visible ligth, 70 mL of 100 ppm MG	97
2	**MoS_2/TiO_2**	40 min, sunlight irradiation, 0.1 g catalyst, 10 ppm MG	97
3	**$PbCrO_4$**	365 ppm MG, 0.1 g catalyst, 4 h, pH=7.5, visible light, 60 min	90
4	**TiO_2/ZnO**	UV light, pH=7, 50 ppm MG, 1.5 g/L catalyst	100
5	**Nix:TiO_2**	25 mL of 10 µM MG, UV light	90
6	**TiO_2**	UV Light, 1 h, 20 mg catalyst, 40 ppm MG	100
7	**V doped-ZnO**	UV and visible lights, 500 ppm MG, 500 ppm catalyst, 200 min	90
8	**$Ni_{1-x}Co_xFe_2O_4$**	Sunlight, 50 mL of 25 ppm catalyst, 1 µM MG, H_2O_2, 15 h	100
9	**$Pt/TiO_2/SiO_2$**	UV and visible lights, 60 min	80
10	**Fe^{3+} doped TiO_2**	UV and visible lights, 5 ppm MG	85
11	**$FeVO_4$**	0.03 g catalyst, UV light, 300 min	90
12	**TiO_2**	UV irradiation, 4 h, 500 ppm catalyst, 50 ppm MG	100
13	**Carbon/TiO_2**	25 ppm MG, 30 min, pH=8	82-100
14	**Mg-doped TiO_2**	Vis light, pH=9, 100 ppm MG	89

the present regression was smaller than 0.05, showing that the model was significant at a high confidence level (95%). A further assessment of the fitted model can be carried out using the lack-of-fit test. Via this statistical test, the residual part is sub-divided into pure error and lack-of-fit. In other words, it distinguishes the random error from the systematic one, causing the lack of fitting of the model with specific order. Therefore, at the 95% confidence level, the p-values for the lack-of-fit should be greater than 0.05, which is not significant. As shown in Table 4, the outcomes of ANOVA are completely in agreement with the above statements.

Also the coefficient of determination (the R-square, adjusted–R-square) was used to express the quality of fit of polynomial model equation. In this case, R^2 of variation fitting for Y%=95 indicated a high degree of correlation between the response and the independent factors (R^2=0.992). Also, the high value of adjusted regression coefficient (R^2-adj=0.984) indicated high significance of the proposed model. This means that, the difference between experimental and the predicted responses is negligible. Also the predicted R-squared value (0.941) was reasonable. It indicates the high accuracy and reliability of the developed mode to determine the response value shown in Fig. 4.

The observed data of the factorial design was fitted to a quadratic response model. Prior to the analysis, low and high factor levels were coded to -1 and +1, respectively. Equation 1 shows the relation between the factors and the yield of the reaction, Y%, based on the first order model:

$$\text{Yield}=76.96888+3420.42741\ H_2O_2+2424.83770\ \text{Catalyst}+2.18670\ \text{Time}+25833.33333\ H_2O_2\times\text{Catalyst}+0.833333\ H_2O_2\times\text{Time}-11.66667\ \text{Catalyst}\times\text{Time}-66934.86448\ H_2O_2^2-25820.45765\ \text{Catalyst}^2-0.016392\ \text{Time}^2$$

Fig. 4a, represents the plot of the predicted versus the experimental degradation efficiency. This figure shows a good agreement between the predicted and experimental degradation efficiency (R^2=0.992) and represents the adequacy and significance of the model. As it is evident in this figure, the obtained data points consistently appear on a straight trend line, demonstrating that there is no obvious dispersal. The directive for selecting the correct power law transformation based on the best lambda is provided by constructing a Box-Cox plot, shown in Fig. 4 b. In this study, the minimum and maximum values of confidence interval are 0.4 and 1.3, respectively. The confidence interval around this lambda includes current point value of 1, which matches the model design value. Normal plot versus studentized residual factor plot shown in Fig. 4c confirms the consistency of the model with the experimental data. Dispersal of residuals is also shown in Fig. 4(d-f). The data reveal that the residuals are in the standard region and so confirm the desirability of the used model to optimize the affecting parameters.

Fig. 5 (a-c) and (d-f) represents the 3D and 2D plots related to the interaction of AB, AC and BC, respectively, at the optimum conditions obtained by design expert software. The data show that the degradation yield is high when the catalyst amount and H_2O_2 volume are 38 mg and 0.03 mL, respectively. In this case, the degradation yield

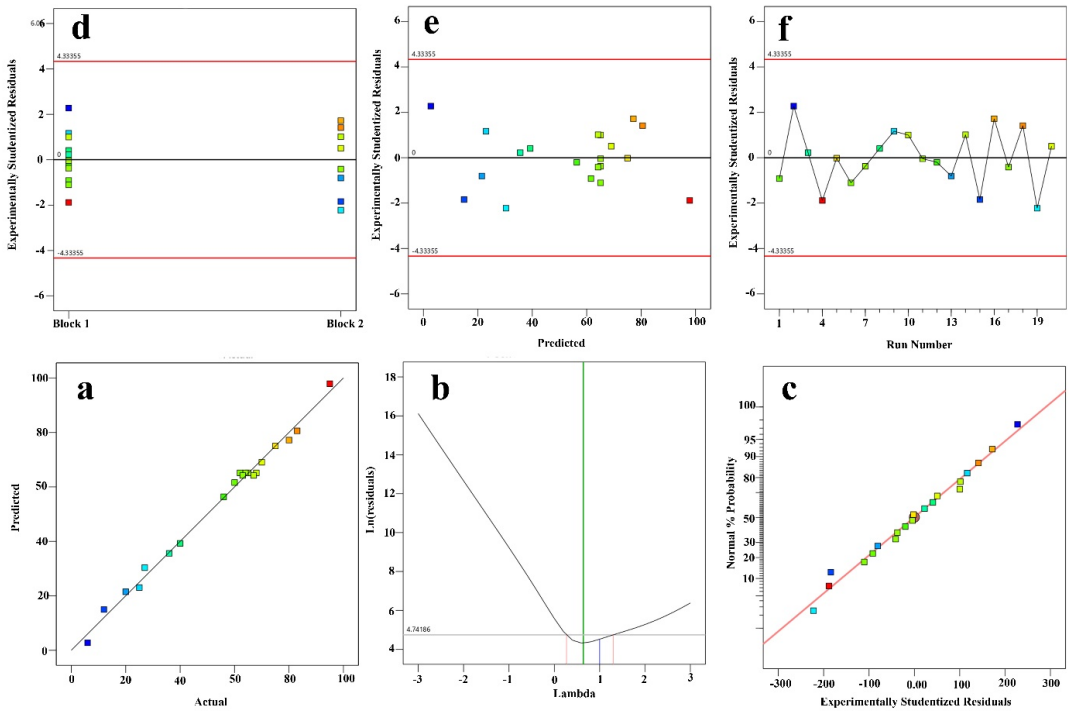

Fig. 4. Plots of a) predicted versus actual, b) lambda, c) the normalized possibility versus studentized residual, d) experimentally studentized residuals versus block, e) experimentally studentized residuals versus predicted efficiency, f) experimentally studentized residuals versus run number.

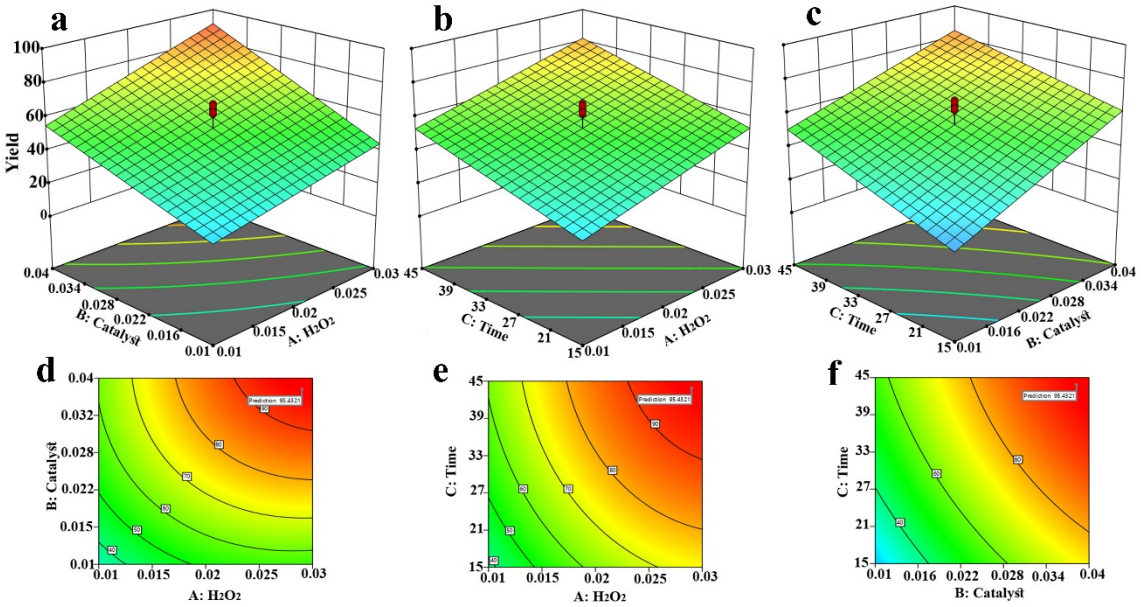

Fig. 5. a-c) 3D and d-f) 2D surface plots extracted from the RSM analysis for the removal of MG dye at the optimized conditions.

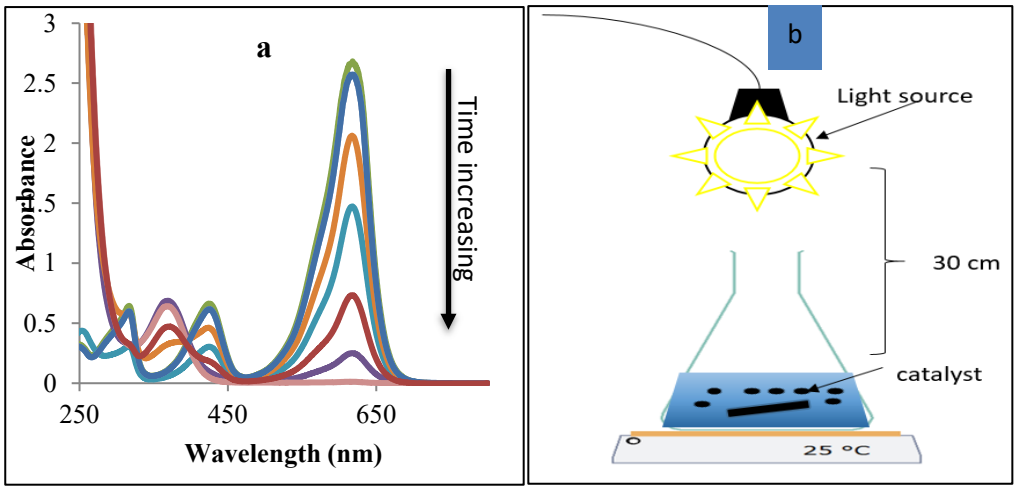

Fig. 6. a) MG degradation spectra, b) schematic images of MG degradation process catalyzed by $NiFe_2O_4$ nanocomposite where the amounts of H_2O_2 and catalyst are 0.03 mL and 0.038 g and time range is 0 to 50 min.

is 95 %. To show the effects of the three factors on the photodegradation process, the response surface methodology (RSM) was used. At a certain reaction time, when H_2O_2 and catalyst amounts increase, dye removal percentage improves. This means that, the mass transfer of dye molecule enhances on the surface of the catalyst and the dye adsorption process on the catalyst reaches equilibrium state quickly. Also, by increasing the catalyst amount, further surface area of adsorbent is available for dyes molecules leads to enhance the dyes removal percentage.

Fig. 6a illustrate the photocatalytic performance of the as-synthesized nanomaterials. Fig. 6 presents MG degradation spectra by $NiFe_2O_4$. The data confirms the high performance of the sample to degrade MG by the mentioned photocatalytic conditions. Fig. 6 b presents a schematic picture for the degradation process of MG at the optimized conditions.

The perturbation plots presented in Fig. 7a demonstrate the comparative effect of all the factors at a particular point in the design space. This plot helps to identify the factor that most influence dye decolourization percentage response. A significant steep slope or curvature of factors A, B and C shows that the decolourization percentage response is sensitive to all factors considered in this study. The higher slope of factor B (amount of catalyst) indicates its high sensitivity to the response. Fig. 7b-d shows a compendium of the simulation results versus the experimental data, including all the runs performed to carry out this work. In this plot the lines corresponding to the 95% Confidence interval and the 95% prediction limits are included. It can be seen that for the system, the agreement is quite satisfactory. Fig. 7e shows Box-Cox plot for power transformations distance plot obtained by the Box-Behnken Design using Cook's distance versus run number, where Cook's distance and studentized residual illustrate the normal distribution and constant variance of the residuals. Box-Cox plot guides us about the selection of an appropriate power transformation of output variables if needed. Cook's distance plot reveals information regarding alteration in regression due to the omission of any experimental run from observed data and suggested for no detection of an outlier. The leverage value of a point equivalent to one specifies that point precisely fits the recorded data (Fig. 7f) and controls the chosen model. All the leverage values were found in permissible limits. DFBETAS vs Run graph determines the impact of each design point on the regression coefficients (Fig. 7g). DFFITS and vs Run graphs (Fig. 7h and 7i) explain the impacts of each design point on the anticipated value.

Fig. 8 a-d presents effects of reaction temperature, run, solution pH and pollutant dyes on the degradation yield at the optimized conditions. As could be found from Fig. 8 a, it is clear that increasing the reaction temperature increases the degradation yield. Fig. 8 b reveals that the catalyst is stable for degradation of MG until run 3. As could be seen from Fig. 8 c, it is found that the degradation yield is high when the

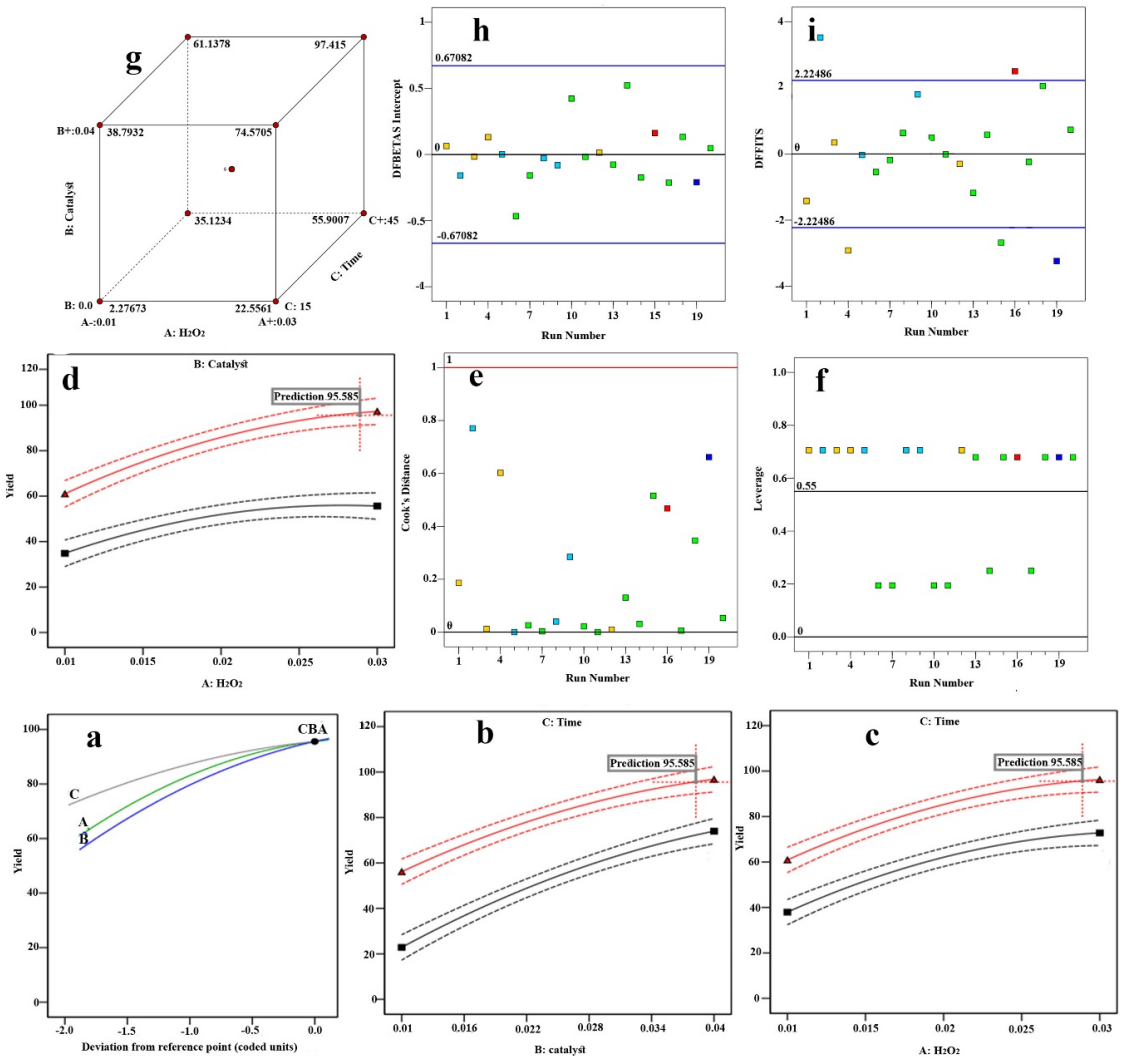

Fig. 7. a) Perturbation plot of operational parameters obtained through RSM, b, c, d) Experimental values plotted against the predicted values derived from the factorial design resulted equations, e) Diagnostic Plots obtained by the Box-Behnken Design showing the interactions among factors, f) leverage versus run number, g) Cube representation showing the standard error of design and interaction effect of factors, h) DFBETAS versus Run number and i) DFFITS versus Run number.

solution pH value is in basic region. According to Fig. 8 d, the performance of $NiFe_2O_4$ to degrade some pollutant dyes at the optimized conditions obtained for the degradation of MG is studied.

Proposed mechanism for photocatalytic degradation

Converting visible light energy to chemical energy in the photocatalysis reaction by $NiFe_2O_4$ could be similar to previously reported and extensively studied mechanism; in a way that electrons (e^-) and holes (h^+) could be excited under visible light irradiation to the conduction and the valence band edge, respectively. These photo-excited e^- and h^+ then can transfer to the surface of the photocatalyst ($NiFe_2O_4$ particles), where they react with oxidants and reductants, respectively, or recombine in the absence of e^- and h^+ traps. The recombination of e^- and h^+ could be greatly minimized in the presence of H_2O_2, which traps the e^- and h^+ to form $^{\bullet}OH$ and $^{\bullet}O_2^-$ species. The excited e^- reacts with H_2O_2 to form $HO^{\bullet}$ and OH^- groups. The formed OH^- group reacts with h^+ and forms $HO^{\bullet}$ group. Besides, H_2O_2 can trap the photoexcited species in another way. It reacts with h^+ and forms $HO_2^{\bullet}$ radical and H^+. The produced $HO_2^{\bullet}$ is decomposed to $^{\bullet}O_2^-$ and H^+. H_2O as the solvent of the photodegradation reaction can

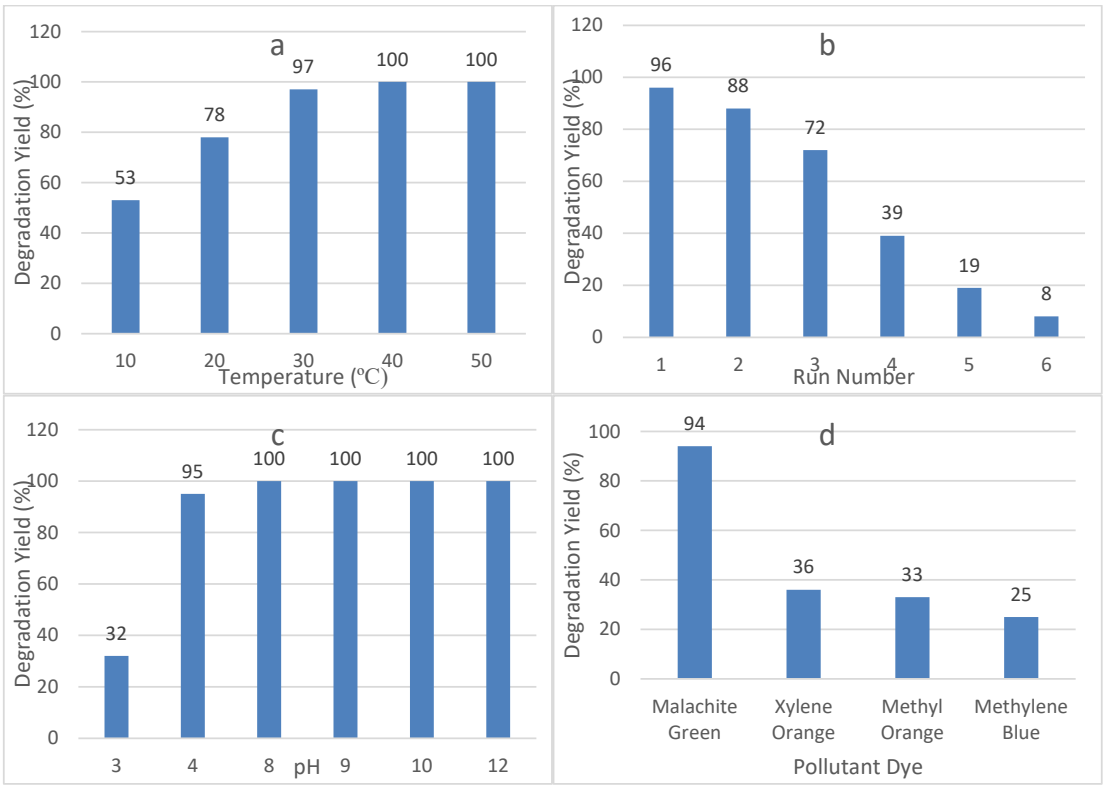

Fig. 8. Plots of a) reaction temperature, b) run number, c) pH and d) pollutant dye effects on the degradation yield at the optimized conditions.

react with h^+ to form $HO^\bullet$ and H^+ species. The produced H^+ ion reacts with the dissolved O_2 and $2e^-$ and forms the initial H_2O_2. The dissolved O_2 can also react with e^- to form $^\bullet O_2^-$. The so-formed $^\bullet OH$ or $^\bullet O_2^-$ species are used for the decomposition of organic contamination molecules such as MG to intermediates or mineralized products through oxidation reactions.

$$NiFe_2O_4 + h\nu \rightarrow h^+ (NiFe_2O_4) + e^- (NiFe_2O_4) \quad (1)$$

$$H_2O_2 + e^- (NiFe_2O_4) \rightarrow HO^\bullet + OH^- \quad (2)$$

$$OH^- + h^+ (NiFe_2O_4) \rightarrow HO^\bullet \quad (3)$$

$$H_2O_2 + h^+ (NiFe_2O_4) \rightarrow HO_2^\bullet + H^+ \quad (4)$$

$$HO_2^\bullet \rightarrow \bullet O_2^- + H^+ \quad (5)$$

$$H_2O + h^+ (NiFe_2O_4) \rightarrow HO^\bullet + H^+ \quad (6)$$

$$2H^+ + O_2 + 2e^- \rightarrow H_2O_2 \quad (7)$$

$$O_2 + e^- (NiFe_2O_4) \rightarrow \bullet O_2^- \quad (8)$$

$$MG + OH^\bullet + \bullet O_2^- \rightarrow \text{degradation product} \quad (9)$$

At high amounts of H_2O_2 volume, the photodegradation yield maybe decreased. It is because the produced highly reactive hydroxyl radical (eq. 11) may react with excess amount of H_2O_2 and produces hydroperoxyl radical ($HO_2^\bullet$) (eq.12) which is less reactive and ultimately inhibits the degradation with producing O_2 and H_2O in (eq.14). The reaction mechanism is explained below:

$$H_2O_2 + e^- (NiFe_2O_4) \rightarrow HO^\bullet + OH^- \quad (10)$$

$$OH^- + h^+ \left(NiFe_2O_4\right) \rightarrow HO^{\bullet} \quad (11)$$

$$H_2O_2 + HO^{\bullet} \rightarrow HO_2^{\bullet} + H_2O \quad (12)$$

$$H_2O_2 + HO_2^{\bullet} \rightarrow HO^{\bullet} + O_2 + H_2O \quad (13)$$

$$HO^{\bullet} + HO_2^{\bullet} \rightarrow O_2 + H_2O \quad (14)$$

To show the merit of the present work, we have compared $NiFe_2O_4$ nanocatalyst results with some of the previously reported catalysts for the degradation of MG (Table 4). It is clear that $NiFe_2O_4$ showed greater activity than some other heterogeneous catalysts. Besides, the data reveal that the high yield of the photodegradation was achieved by the application of visible light condition in this work.

CONCLUSION

In the present study, Hirshfeld analysis and photocatalytic performance of $NiFe_2O_4$ to remove pollutant dye were investigated. It was found from Hirshfeld surface analysis that the Ni-O, Ni-Ni, O-Ni, O-O contacts are presented as red spots on the corresponded HS. In additional, the different intermolecular contacts' small percentage interactions were determined by a 2D fingerprint plot. The photocatalytic data indicated that the obtained materials had excellent efficiency for the removal of MG from aqueous solution. It was found that the optimum condition was 0.04 mL H_2O_2, 30 mg catalyst and 35 min reaction time. The degradation yield at the optimized conditions was 95 %.

CONFLICTS OF INTEREST

All authors have read and declare no conflict of interest.

REFERENCE

[1] Kesavan A. G., Nataraj N., Chen S. M., Lin L. H., (2020), Hydrothermal synthesis of $NiFe_2O_4$ nanoparticles as an efficient electrocatalyst for the electrochemical detection of bisphenol. *New J. Chem*. 44: 7698-7707.

[2] Sivakumar P., Ramesh R., Ramanand A., Ponnusamy S., Muthamizhchelvan C., (2013), Synthesis and characterization of $NiFe_2O_4$ nanoparticles and nanorods. *J. Alloys Compd*. 563: 6-11.

[3] Amulya M. A. S., Nagaswarupa H. P., AnilKumar M. R., Ravikumar C. R., Prashantha S. C., Kusuma K. B., (2020), Sonochemical synthesis of $NiFe_2O_4$ nanoparticles: Characterization and their photocatalytic and electrochemical applications. *Appl. Surf. Sci. Adv*. 1: 100023-100026.

[4] Naidu K. C. B., Madhuri W., (2017), Hydrothermal synthesis of $NiFe_2O_4$ nano-particles: structural, morphological, optical, electrical and magnetic properties. *Bull. Mater. Sci*. 40: 417-425.

[5] Xia Y., Yang P., Sun Y., Wu Y., Mayers B., Gates B., Yin Y., Kim F., Yan H., (2003), One-dimensional nanostructures: Synthesis, characterization, and applications. *Adv. Mater*. 15: 353-389.

[6] Yue W., Changhong S., Wei Y., (2010), Fabrication and magnetic properties of $NiFe_2O_4$ nanorods. *Rare Metals*. 29: 385-389.

[7] Raj K., Moskowitz B., Casciari R., (1995), Advances in ferrofluid technology. *J. Magn. Magn. Mater*. 149: 174-180.

[8] Wang J., Zhua Y. J., Lia W. P., Chen Q. W., (2005), Necklace-shaped assembly of single-crystal $NiFe_2O_4$ nanospheres under magnetic field. *Mater. Lett*. 59: 2101-2103.

[9] Reddy D. H. K., Yunang Y. S., (2016), Spinel ferrite magnetic adsorbents: alternative future materials for water purification. *Coord. Chem. Rev*. 315: 90–111.

[10] Ishino K., Narumiya Y., (1987), Development of magnetic ferrites: control and application of Losses. *Ceram. Bull*. 66: 1469–1475.

[11] Srivastava S., Sinha R., Roy D., (2004), Toxicological effects of malachite green. *Aquatic toxicol*. 66: 319-329.

[12] Tolia J., Chakraborty M., Murthy Z., (2012), Photocatalytic degradation of malachite green dye using doped and undoped ZnS nanoparticles. *Pol. J. Chem. Technol*. 14: 16-21.

[13] Chen C., Lu C., Chung Y., Jan J., (2007), UV light induced photodegradation of malachite green on TiO_2 nanoparticles. *J. Hazard. Mater*. 141: 520-528.

[14] Kusuma H. S., Sholihuddin R. I., Harsini M., Darmokoesoemo H., (2016), Electrochemical degradation of malachite green dye using Carbon/TiO_2 electrodes. *J. Mater. Environ. Sci*. 7: 1454-1460.

[15] Miranzadeh M., Afshari F., Khataei B., Kassaee M., (2020), Adsorption and photocatalytic removal of arsenic from water by a porous and magnetic nanocomposite: Ag/TiO_2/Fe_3O_4@GO. *Adv. J. Chem. A*. 3: 408-421.

[16] Sajjadnejad M., Karimi Abadeh H., (2020), Processing of nanostructured TiO_2 and modification of its photocatalytic behavior for methylene blue degradation. *Adv. J. Chem. A*. 3: 422-431.

[17] Hu K.-h., Meng M., (2013), Degradation of malachite green on MoS_2/TiO_2 nanocomposite. *Asian J. Chem.* 25: 5827-5829.

[18] Ameta K., Tak P., Soni D., Ameta S. C., (2014), Photocatalytic decomposition of malachite green over lead chromate powder. *Sci. Rev. Chem. Commun*. 4: 38-45.

[19] Bansal P., Bhullar N., Sud D., (2009), Studies on photodegradation of malachite green using TiO_2/ZnO photocatalyst. *Desalin. Water Treat*. 12: 108-113.

[20] Soni H., JI N. K., (2014), UV light induced photocatalytic degradation of malachite GREEN on TiO_2 nanoparticles.

Int. J. Recent Res. Rev. 7: 10-15.

[21] Sols-Casados D., Escobar-Alarcn L., Fernndez M., Valencia F., (2013), Malachite green degradation in simulated wastewater using Ni_x : TiO_2 thin films. *Fuel*. 110: 17-22.

[22] Khezami L., Taha K. K., Ghiloufi I., El Mir L., (2016), Adsorption and photocatalytic degradation of malachite green by vanadium doped zinc oxide nanoparticles. *Water Sci. Technol*. 73: 881-889.

[23] Jo W.-K., Parka G. T., Tayade R. J., (2014), Synergetic effect of adsorption on degradation of malachite green dye under blue LED irradiation using spiral-shaped photocatalytic reactor. *J. Chem. Technol. Biotechnol*. 90: 2280-2289.

[24] He H-Y., (2015), Photocatalytic degradations of malachite green on magnetically separable $Ni_{1-x}Co_xFe_2O_4$ nanoparticles synthesized by using a hydrothermal process. *Amer. Chem. Sci. J.* 6: 58-68.

[25] Afshar S., Samari Jahromi H., Jafari N., Ahmadi Z., Hakamizadeh M., (2011), Degradation of malachite green oxalate by UV and visible lights irradiation using $Pt/TiO_2/SiO_2$ nanophotocatalyst. *Sci. Iran*. 18: 772-779.

[26] Khademinia S., Behzad M., Kafi-Ahmadi L., Hadilou S., (2018), Hydrothermally synthesized strontium arsenate nanomaterial through response surface methodology. *Z. Anorg. Allg. Chem*. 644: 221-227.

[27] Azari B., Pourahmad A., Sadeghi B., Mokhtary M., (2019), Preparation and photocatalytic study of SiO_2/CuS core-shell nanomaterial for degradation of methylene blue dye. *Nanomeghyas*. 3: 103-114.

[28] Hajavazzade R., Kargar Razi M., Mahjoub A. R., (2021), Synthesis and characterization of $Mg_{1-x}Ni_xAl_2O_4$ and their photocatalytic behaviors towards Congo red under UV light irradiation. *Int. J. Nano Dimens*. 12: 67-75.

[29] Blourfrosh S. K., Mahanpoor K., (2021) Preparation, characterization and photocatalytic performance of nano α-Fe_2O_3 supported on metal organic framework of Cd(II) for decomposition of Cefalexin aqueous solutions. *Int. J. Nano Dimens*. 12: 113-127.

[30] Hosseiny Davarani S. S., Rezayati Zad Z., Taheri A. R., Rahmatian N., (2017), Highly selective solid phase extraction and preconcentration of Azathioprine with nano-sized imprinted polymer based on multivariate optimization and its trace determination in biological and pharmaceutical samples. *Mater. Sci. Eng. C.* 71: 572–583.

[31] Abdollahi F., Taheri A., Shahmari M., (2020), Application of selective solid-phase extraction using a new core-shell-shell magnetic ionimprinted polymer for the analysis of ultra-trace mercury in serum of gallstone patients. *Sep. Sci. Technol.* 55: 2758-2771.

[32] Hakimyfard, A., Khademinia, S., (2021), Structural, Magnetic, Optical and Electrochemical Properties of a New Class of α-Fe_2O_3-M_x-$NiFe_2O_{4+\delta}$ (M = None, Co^{2+}, Eu^{3+}, Ho^{3+} and Yb^{3+}) Nanocomposites. *J. Supercond. Nov. Magn.* 34: 1-9.

[33] Turner M. J., McKinnon J. J., Wolff S. K., Grimwood D. J., Spackman P. R., Jayatilaka D., Spackman M. A., (2017). Crystal Explorer 17.5. *The University of Western Australia.*

[34] Seth S. K., Saha N. C., Ghosh S., Kar T., (2011), Structural elucidation and electronic properties of two pyrazole derivatives: a combined X-ray, Hirshfeld surface analyses and quantum mechanical study. *Chem. Phys. Lett*. 506: 309-314.

[35] McKinnon J. J., Jayatilaka D., Spackman M. A., (2007), Towards quantitative analysis of intermolecular interactions with Hirshfeld surfaces. *Chem. Commun*. 3814-3816.

[36] Spackman M. A., McKinnon J. J., (2002), Fingerprinting intermolecular interactions in molecular crystals. *Cryst. Eng. Comm*. 4: 378-392.

[37] Fabbiani F. P. A., Leech C. K., Shankland K., Johnston A., Fernandes P., Florence A. J., Shankland N., (2007), Hirshfeld surface analysis of two bendroflumethiazide solvates. *Acta Crystallogr. Sect*. C. 63: 659-663.